Available online at www.sciencedirect.com
ScienceDirect
Journal of the European Ceramic Society 31 (2011) 2247–2254
www.elsevier.com/locate/jeurceramsoc

Influence of pulse current during Spark Plasma Sintering evidenced on reactive alumina–hematite powders

Julien Gurt Santanach [a], Claude Estournès [a], Alicia Weibel [a], Geoffroy Chevallier [a], Vincent Bley [b], Christophe Laurent [a], Alain Peigney [a,*]

[a] Université de Toulouse, Institut Carnot CIRIMAT, UMR CNRS-UPS-INP 5085, Université Paul-Sabatier, 118 route de Narbonne, 31062 Toulouse Cedex 9, France
[b] Université de Toulouse, LAPLACE, UMR CNRS-UPS-INP 5213, Université Paul-Sabatier, 118 route de Narbonne, 31062 Toulouse Cedex 9, France

Received 28 March 2011; received in revised form 30 May 2011; accepted 7 June 2011
Available online 29 June 2011

Abstract

Spark Plasma Sintering (SPS) is increasingly used. The temperature and current are not independent parameters, making it difficult to separate the current intrinsic role from Joule heating. There is a debate on whether there are any specific SPS mechanisms. The influence of a key parameter, the (on:off) pulse pattern, is studied on the SPS of reactive α-$Al_{2-2x}Fe_{2x}O_3$ ($x = 0.02$; 0.05; 0.07; 0.10) powders. Changing it modifies the current crest intensity and has a great influence on the materials microstructure. Comparisons with runs where the current is blocked and hot-pressing reveal three competing phenomena: formation of $FeAl_2O_4$, dominant in the core and not peculiar to SPS, formation of Fe, producing Fe-Al_2O_3 composite surface layers, and most notably electrical-field induced diffusion of Fe^{3+} ions towards the cathode, which could have far-ranging implications for the consolidation of ionic materials and the *in situ* reactive shaping of composites and multimaterials.

Keywords: Spark Plasma Sintering; A. Hot pressing; B. Nanocomposites; B. Electron microscopy; Fe-Al_2O_3

1. Introduction

Spark Plasma Sintering (SPS)[1] is becoming increasingly popular for the preparation of many materials, including ionic materials,[2–8] because it has several advantages over pressureless sintering and hot-pressing, including lower sintering temperatures and shorter holding times. SPS typically differs from hot-pressing by the application of a DC pulsed current to the pressing die and sample. The temperature and current are not independent parameters and it may be difficult to separate the intrinsic role of the current from its thermal effect, *i.e.* Joule heating. Therefore, there is a debate on whether there are any mechanisms specific to SPS.[9–22] Reviews of the field[2,19] show that most papers report results on the densification of nanomaterials with little grain growth or on materials bonding, with or without a reaction at the interface. Several authors[15–22] investigate the SPS process of model materials, conducting or insulating, but our approach is to investigate it via the sintering of a reactive powder. It was shown[23] that SPS of nanocomposite powders such as Fe-$Al_{2-2x}Fe_{2x}O_3$ produces materials with a surface-layer composition and microstructure different to that of the core. Increasing the thickness of the Fe-Al_2O_3 surface layer provoked an increase in both Vickers microhardness and fracture strength. The aim of this paper is to get a better understanding of the processes involved in SPS, using the reactive sintering of α-$Al_{1.86}Fe_{0.14}O_3$ (corundum-type structure), by studying the influence of a key SPS parameter, the (on:off) pulse pattern. This is compared with experiments where the current path is blocked and also with hot-pressing. Moreover, the influence of the sample composition (iron ions content of the starting oxide) is investigated.

2. Experimental procedure

2.1. Powder synthesis

For the first part of the study, a powder of α-$Al_{1.86}Fe_{0.14}O_3$ solid solution (corundum-type structure) was prepared by the mixed-oxalate precipitation/calcination route.[24] The calcination

* Corresponding author. Tel.: +33 05 61 55 61 75; fax: +33 05 61 55 61 63.
E-mail address: peigney@chimie.ups-tlse.fr (A. Peigney).

0955-2219/$ – see front matter © 2011 Elsevier Ltd. All rights reserved.
doi:10.1016/j.jeurceramsoc.2011.06.003

(air, 1200 °C, 2 h) produced a powder in which micrometric grains presenting a vermicular microstructure form agglomerates 15–20 μm in size. The BET specific surface area is equal to 2.3 m^2/g. It was verified by X-ray diffraction (XRD) that only the peaks typical of the corundum-type oxide are present and that no $FeAl_2O_4$ is present. The powder was divided into seven batches, as required for the study. In addition, α-$Al_{2-2x}Fe_{2x}O_3$ powders with different iron contents were prepared by the same route. Two of them ($x = 0.02$ and 0.05) contain less iron than the previous one ($x = 0.07$) and are made up solely of the corresponding α-$Al_{2-2x}Fe_{2x}O_3$ solid solution. For a higher iron content ($x = 0.10$), XRD reveals traces of a hematite-rich solid solution (α_2) in addition to the alumina-rich solid solution (α_1), which indicates[24] that the saturation (of hematite dissolved into alumina) was reached for this sample (*i.e.* that the limit of substituting Fe^{3+} ions for Al^{3+} ions in the corundum lattice is reached).

2.2. Spark Plasma Sintering (SPS) and hot-pressing

Three α-$Al_{1.86}Fe_{0.14}O_3$ ($x = 0.07$) powder batches were consolidated by SPS (Dr Sinter 2080, SPS Syntex Inc., Japan). They were loaded into an 8 mm inner diameter graphite die. A sheet of graphitic paper was placed between the punch and the powder as well as between the die and the powder for easy removal. This ensemble is known as the stack. The powders were sintered under vacuum (residual cell pressure lower than 5 Pa). A heating rate of 250 °C/min was used from room temperature to 600 °C, where a hold of 1 min was applied in order to stabilize the temperature reading. Then, a heating rate of 250 °C/min was used from 600 to 1350 °C, where a 3-min dwell at 1350 °C was applied. An optical pyrometer, focused on a little hole at the surface of the die, was used to measure and monitor the temperature. The uniaxial pressure was gradually applied up to 100 MPa within the first minute of the dwell at 1350 °C and maintained at 100 MPa during the remaining 2 min. The cooling rate was close to 600 °C/min for the first minute and then was natural. The uniaxial pressure was gradually released during cooling. The heat-treatment described above was performed using three different (on:off) pulse patterns: (12:2), (2:2) and (2:6), each pulse corresponding to 3.3 ms, producing materials denoted A7, B7 and C7, respectively (Table 1). Note that (12:2) is the default pattern of the machine. For the second part of the study, the powders with different iron contents ($x = 0.02$, 0.05 and 0.10) were consolidated by SPS in the same conditions as specimen C7, producing samples C2, C5 and C10, respectively (Table 1). The next part aimed at investigating the influence of a higher temperature and a longer treatment time. Thus, specimen D7 was consolidated using the (12:2) pulse pattern, but with a much lower heating rate (20 °C/min), up to a higher temperature (1450 °C), where a longer dwell (15 min) was applied (Table 1). A pressure of 43 MPa was applied during the heating ramp. These conditions for D7 were chosen to be similar to that used for a sample prepared by hot-pressing (see below). For the last part of the study, three more specimens were prepared using the remaining α-$Al_{1.86}Fe_{0.14}O_3$ powder batches: specimen E7 (Table 1) was consolidated by SPS in the same conditions as A7, except that on each side of the stack, an alumina powder bed about 1.5 mm thick was placed between the punches and the graphite paper disks, which moreover were smaller in diameter than the punches (*i.e.* they did not cover the outer radial part of the powder and did not make contact with the die). Specimen F7 (Table 1) was consolidated in the same conditions as E7 but the graphite paper disks were removed altogether, in order to block any axial current flow in the material. Finally, specimen G7 (Table 1) was prepared by hot-pressing (Astro Industries, USA) at 1450 °C using a cycle similar to that used for D7. All materials inside the hot-pressing cell (resistor, felts, stack, punches) are in graphite and full-size graphite paper disks were present.

2.3. Characterization

The sintered specimens were in the form of pellets 8 mm in diameter and about 2 mm thick. The density was determined using Archimedes method after removal of the graphitic surface contamination layer by light polishing. The density is in the range of 3.9–4.0 for all specimens, which corresponds to a densification in the range of 98–100%. The specimens were cut in their middle along the pressing axis using a diamond blade. One half was used as a cross-section and was polished up to a 1 μm diamond suspension. The cross-sections were observed by field-emission-gun scanning electron microscopy (FESEM, JEOL JSM 6700F). The other half was used for X-ray diffraction

Table 1
Samples, iron content in the starting α-$Al_{2-2x}Fe_{2x}O_3$ powder (x) and consolidation experimental conditions: SPS pulse pattern (on:off), maximum temperature (T), heating rate (r) from 600 °C to T, dwell time (t) at T, uniaxial pressure (P). Remarks: see text for details. GDP: graphite paper disks.

Sample	x	(on:off)	T (°C)	r (°C/min)	t (min)	P (MPa)	Remarks
A7	0.07	(12:2)	1350	250	3	100	–
B7	0.07	(2:2)	1350	250	3	100	–
C7	0.07	(2:6)	1350	250	3	100	–
C2	0.02	(2:6)	1350	250	3	100	–
C5	0.05	(2:6)	1350	250	3	100	–
C10	0.10	(2:6)	1350	250	3	100	–
D7	0.07	(12:2)	1450	20	15	43	Longer SPS treatment, similar to HP
E7	0.07	(12:2)	1350	250	3	100	Al_2O_3 barriers, small diameter GPD
F7	0.07	(12:2)	1350	250	3	100	Al_2O_3 barriers, no GPD
G7	0.07	–	1450	20	15	43	HP

Table 2
Samples, crystallized compounds detected by XRD in the composite layer and in the core (Fe = α-Fe, A = α-Al_2O_3, SP = $FeAl_2O_4$), composite layer thickness and depletion layer (DL) thickness at the top and bottom sides of the specimen; no: not present; nm: not measured; GDP: graphite paper disks.

Sample	Composite layer (XRD)	Composite layer thickness top (μm)/bottom (μm)	DL thickness top (μm)/bottom (μm)	Core (XRD)
A7	Fe + A	38/32	Ill-defined/no	SP + A
B7	Fe + A	48/32	Well-defined/no	SP + A
C7	Fe + A	48/32	9/no	SP + A
C2	Fe + A	20/nm	11/no	SP + A
C5	Fe + A	31/nm	7/no	SP + A
C10	Fe + A	55/nm	Ill-defined/no	SP + A
D7	Fe + A	20/64[a]	25/20[a]	SP + A
E7	Fe + A, below GPD/SP + A, when no GPD	nm	No/no	SP + A
F7	SP + A	No/no	No/no	SP + A
G7	SP + A (Fe + A in some places)	Irregular	No/no	SP + A

[a] Reversed positions compared to other samples. See text for details.

(XRD) (Cu K_α radiation, Bruker D4 Endeavor) investigations performed on the semi-circular surfaces, first on the unpolished one, then on samples ground ever deeper, in order to reveal the crystallized phases present at various depths into the material.

3. Results and discussion

3.1. Influence of the pulse pattern

The results presented below, obtained by XRD patterns analysis and FESEM observations, are summarized in Table 2. A visual examination of the cross-sections of specimens A7, B7 and C7 (Table 1) revealed a difference in color, as already observed previously[23]: a gray color for the surface and a green color for the core of the sample. The XRD patterns (not shown) of the unpolished specimens revealed α-Fe and α-Al_2O_3 peaks and very weak Fe_3C peaks. The specimens were slightly ground and only α-Fe and α-Al_2O_3 were detected, suggesting that Fe_3C was produced by reaction between Fe and the graphite paper disk. After some more grinding, only $FeAl_2O_4$ and α-Al_2O_3 were detected. FESEM images (back-scattered electron images in chemical contrast mode) of the cross-sections (top side of the specimens, close to the upper punch, *i.e.* the cathode) show Fe (white dots) and $FeAl_2O_4$ particles (light-gray) on a dark-gray background of the corundum-phase matrix (Fig. 1). The average thickness of the composite layer is about 38 μm for A7 and *ca.* 48 μm for B7 and C7. The Fe particles are equiaxed for A7 and B7 (diameter 0.5–0.8 μm) and appear larger and elongated (maximum length *ca.* 5 μm) for C7. Regarding the core, the $FeAl_2O_4$ and Al_2O_3 grains are much coarser for C7. Interestingly, the composite layer is separated from the core by a layer without any Fe particles or $FeAl_2O_4$ grains. This so-called depletion-layer (DL) is ill-defined (or non-existing at some places) for A7, more clearly detected for B7 and very prominent for C7 (*ca.* 9 μm thick). For the bottom side, the thickness of the composite layer is about 32 μm for all three samples and no DL is observed, although care was exercised for the precise positioning of the sample within the stack. On the peripheral surface of the specimen (*i.e.* the area close to the die), the Fe-Al_2O_3 layer is also observed for all three specimens and no DL is observed.

3.2. Influence of the iron content

Typical FEG-SEM images of the top sides (Fig. 2) of specimens C2, C5 and C10 (Table 1) revealed a microstructure similar to that observed for C7, notably for C2 (Fig. 2a) and C5 (not shown). For C10, the DL is ill-defined or non-existing (Fig. 2b and c). The thickness of the composite layer increases (up to about 55 μm) upon the increase in iron content, whereas by contrast the average thickness of the DL tends to slightly decrease (Fig. 3).

3.3. Influence of the temperature and duration

For D7 (Table 1), compared to A7, at the top side (Fig. 4a), the composite layer is thinner (20 μm) and the DL is clearly defined and very thick (25 μm). At the bottom side (Fig. 4b), most interestingly, the DL (*ca.* 20 μm thick) is observed close to the punch and is separated from the core by the composite layer (*ca.* 64 μm thick), the microstructure of which is moreover different from the other ones observed so far, showing a lower density of larger Fe particles.

3.4. Current-blocking in SPS and hot-pressing

The part of specimen E7 (Table 1) that was below the graphite paper disk (noted GPD in Fig. 5) is similar to specimen A7, the thickness of the Fe-Al_2O_3 layer decreasing when one gets closer to the edge of the disk (*i.e.* the place where the graphite paper disk ends) (Fig. 5a). By contrast, no such layer is observed in the areas where the powder was directly in contact with alumina, which was difficult to separate from the material (arrowed on the image) due to strong diffusion-bonding. Thus, for this part of E7, the whole material is made up of $FeAl_2O_4$ and Al_2O_3. The same is observed (Fig. 5b) for all areas of specimen F7 (Table 1). Specimen G7, prepared by hot-pressing (Table 1), contains $FeAl_2O_4$ and Al_2O_3 and the composite surface layer,

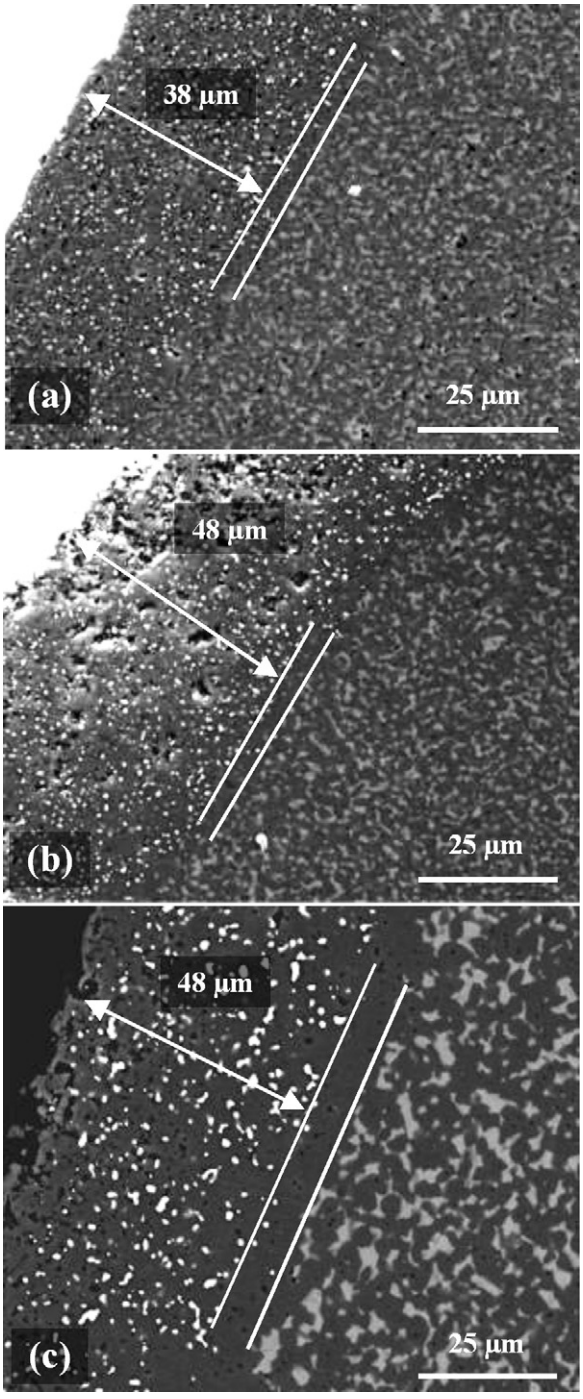

Fig. 1. FESEM images of a cross-section (top side) of specimens (7 cat.% Fe, $x = 0.07$) prepared by SPS with different pulse patterns (on:off): (a) A7, (12:2); (b) B7, (2:2); and (c) C7, (2:6).

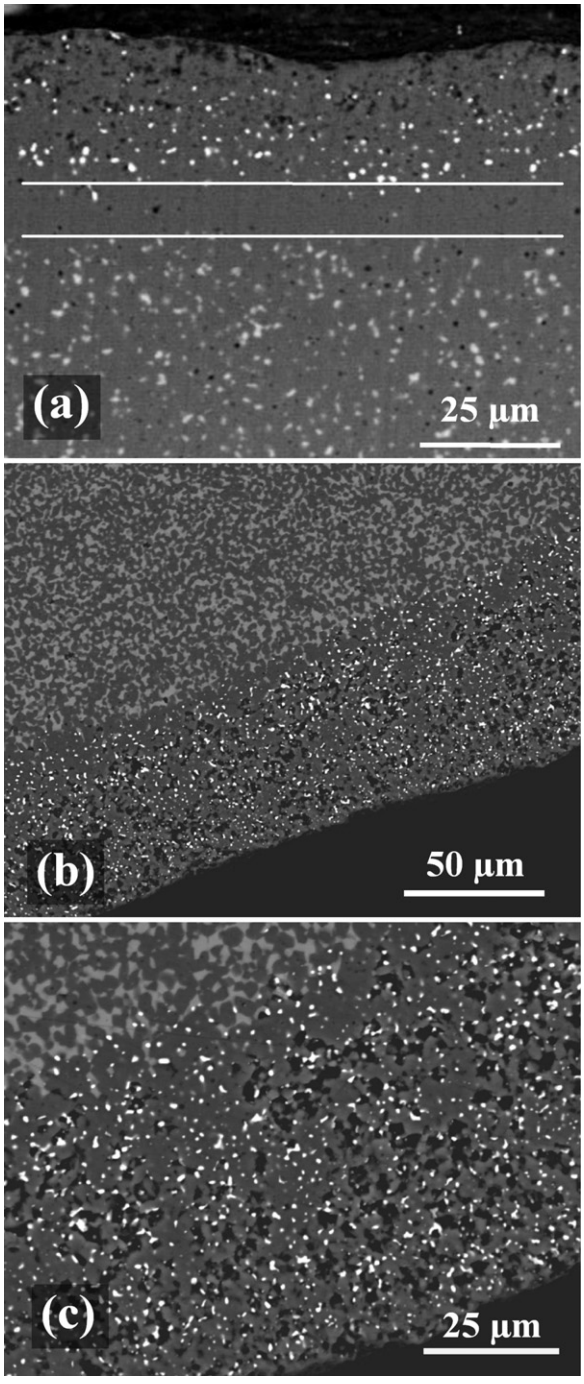

Fig. 2. FESEM images of a cross-section (top side) of specimens with different iron contents prepared by SPS with a (2:6) pulse pattern: (a) C2 ($x = 0.02$); (b) and (c) C10 ($x = 0.10$).

when present, is much less regular than for the SPS samples (Fig. 5c–e).

3.5. Discussion

The formation of $FeAl_2O_4$, of the DL and of the Fe-Al_2O_3 composite layer and their respective positions within the specimens will be discussed. Firstly, the consequence of changing the pulse pattern on the crest intensity of the current will be examined. The waveform of the "on" period is composed of several pulses.[25] The number of pulses per second calculated from the ratio of the number of pulses and the total pattern duration is equal to 260, 152 and 76 for the (12:2), (2:2) and (2:6) patterns, respectively. The intensity delivered by the SPS generator to heat the stack at 1350 °C was recorded using a magneto-electric amperometer. The evolution (528, 436 and 432 A for the (12:2), (2:2) and (2:6) patterns, respectively) is in agreement with earlier results[25] and we propose that this could mean that the SPS

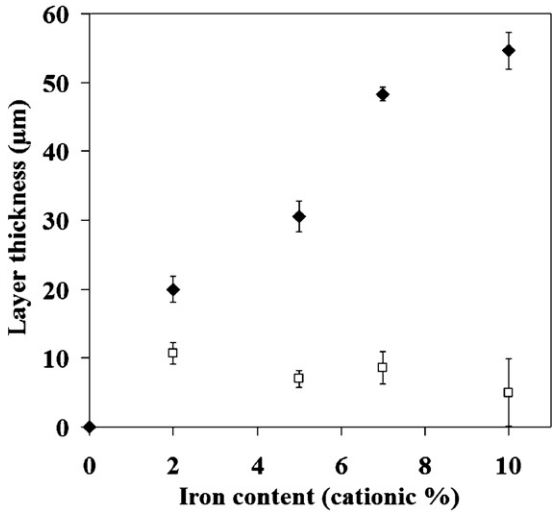

Fig. 3. Thickness of the Fe-Al_2O_3 top-side composite surface layer (solid diamonds) and of the depletion layer (open squares) versus the iron content for specimens prepared by SPS with a (2:6) pulse pattern.

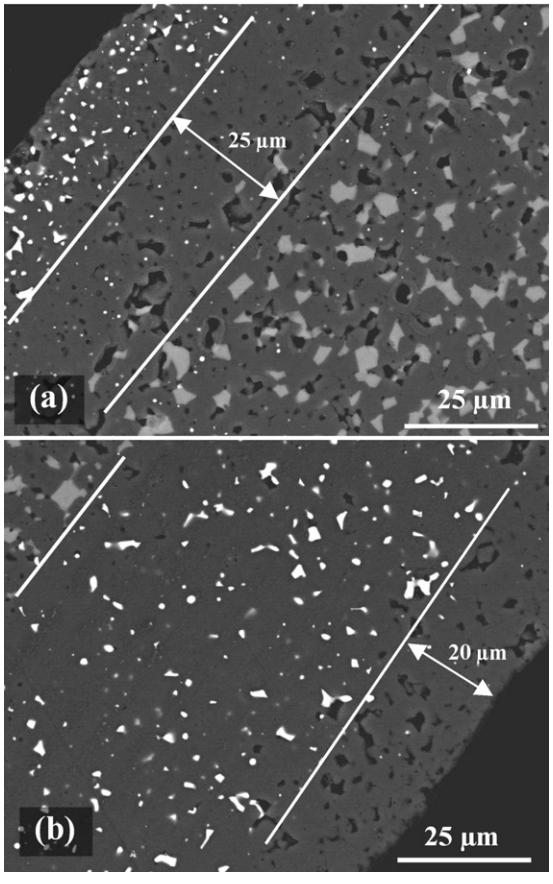

Fig. 4. FESEM images of a cross-section of specimen D7 (7 cat.% Fe, $x = 0.07$) prepared by SPS with a (12:2) pulse pattern, but using a lower heating rate, a higher temperature and for a longer dwell time than all other samples, showing (a) the top side, close to the upper punch (*i.e.* the cathode) and (b) the bottom side.

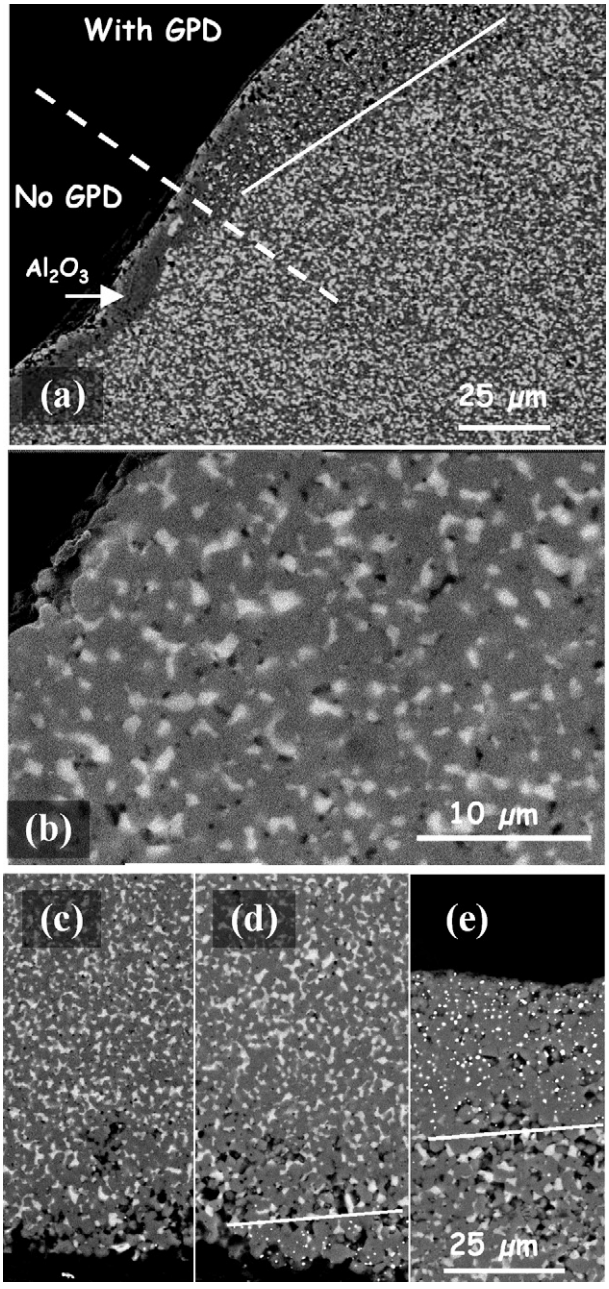

Fig. 5. FESEM images of a cross-section (top side) of (a) specimen E7 and (b) specimen F7 prepared by SPS in different current-blocking conditions (see text for details) and (c–e) specimen G7 prepared by hot-pressing. GPD = graphite paper disk.

is not a simple resistive but a partially inductive system. From the mean intensity values, it is deduced that during one second of pulse current, the delivered electric charges are 528, 436 and 432 C and thus that the corresponding crest intensity (I_c) for each pulse (*i.e.* for each 3.3 ms "on" period, considering each pulse as rectangular) is equal to 615, 869 and 1722 A, respectively, showing a great influence of the pulse pattern. The crest voltages were measured and found between about 10 V for (12:2) and about 20 V for (2:6). These values are to be considered as averages, because the pulses in a given train are neither the same in voltage nor in current intensity.[25]

The formation of $FeAl_2O_4$ is observed for all specimens, prepared by SPS or hot-pressing, showing that it is not peculiar to SPS. It is proposed that it occurs by phase partitioning as described by reaction (1),[23] which is a consequence of the high temperature and low $P(O_2)$.[26]

$$Al_{1.86}Fe_{0.14}O_3 \rightarrow 0.14FeAl_2O_4 + 0.79Al_2O_3 + 0.035O_2 \quad (1)$$

The higher size of the $FeAl_2O_4$ grains for C7 (compared to A7 and B7) reflects a higher rate of phase partitioning, suggesting a higher temperature in the core because of the higher I_c. The presence of $FeAl_2O_4$ extends to all areas of the specimens that are not in close proximity to the surrounding graphite from either the die or graphite paper because reaction (1) competes with the formation of the Fe-Al_2O_3 composite layer, which will be discussed later.

Let us try before to explain the formation of the DL. For A7, B7 and C7, the DL is thicker when I_c is higher on the top side of the samples (Fig. 1) but not on the bottom side. An explanation that was considered to explain the asymmetry is that the bottom side (*i.e.* the anode) may experience a lower temperature due to the axially asymmetric current flow.[27] However, considering that the specimen is thin (<3 mm), the temperature of the surrounding graphite die is probably identical along the length of the specimen, and thus the difference between the top- and bottom-side temperatures is probably low. Moreover, a DL is present at the very bottom of sample D7 prepared like A7 but at a higher temperature and with a much longer treatment. This suggests that there were no remaining Fe^{3+} ions at the bottom of D7 to form either $FeAl_2O_4$ or Fe and therefore points towards upward diffusion. Taking into account the crest voltages and the low thickness of the samples, it is proposed that the electrical field is sufficiently high to activate the diffusion of iron ions, most probably Fe^{3+} ions, towards the cathode. Shen et al.[9] reported that both grain-boundary diffusion and grain-boundary migration are enhanced by the electrical field originating from the pulsed current. For D7, this phenomenon has time to take place before the reduction of iron species to Fe, but not so for C7 (and all the more so for A7 and B7), thus explaining that there is no DL at the bottom side for A7, B7 and C7. The thicker top-side DL for C7 compared to A7 and B7 could reflect that the Fe^{3+} ions supply is stopped because, as mentioned above, higher bulk temperatures achieved for C7 due to higher I_c and crest voltage, would favor a higher phase partitioning rate in the core, producing more $FeAl_2O_4$. This implies that the Fe^{2+} ions are not involved on the upwards diffusion process and thus are not necessarily involved in the formation of Fe (as discussed below), because otherwise $FeAl_2O_4$ would be detected in the DL. Thus, there is a competition between the formation of $FeAl_2O_4$ by reaction (1), which also corresponds to a reduction of Fe^{3+} into Fe^{2+} ions, and electrical field-induced Fe^{3+} diffusion. Using a pulse pattern with high I_c and crest voltage such as (2:6) favors the former for rapid treatments because it allows for higher temperatures to be reached in the bulk of the sample but favors the latter for slow treatments.

There is a competition of reaction (1) with the formation of the Fe-Al_2O_3 composite layer, which can occur via reactions (2) and/or (3).[23]

$$FeAl_2O_4 \rightarrow Fe + Al_2O_3 + (1/2)O_2 \quad (2)$$

$$Al_{1.86}Fe_{0.14}O_3 \rightarrow 0.14Fe + 0.93Al_2O_3 + 0.105O_2 \quad (3)$$

Note that (3) corresponds to a direct reduction of Fe^{3+} ions into Fe obviating the Fe^{2+} ions ($FeAl_2O_4$) intermediates and thus reaction (2). For the H_2 reduction of similar solid solutions,[28,29] Fe is formed either directly or via $FeAl_2O_4$ for temperatures higher or lower than 1000 °C, respectively. It is probable that at the present temperatures, (3) is preeminent, supporting the above proposition that $FeAl_2O_4$ is not involved in the formation of Fe. From the current-blocking experiments (E7 and F7), it appears clearly that the absence of graphite paper prevents the formation of the composite layer, showing that these conditions are more favorable to the formation of $FeAl_2O_4$ by (1).

With the graphite paper, SPS, but not hot-pressing, leads to a Fe-Al_2O_3 layer of a fairly regular thickness on the top and bottom sides of the specimens, pointing towards some characteristic effect(s). Moreover the top composite layer is thicker when using a higher I_c. This could reflect that for SPS the top side of the specimen is continuously supplied by Fe^{3+} ions through field-induced diffusion, as long as the formation of $FeAl_2O_4$ has not started. Specimen A7 can be compared to our previously studied sample (codenamed R0S in Ref. 23), for which the composite layer thickness was only 10 μm. The same sintering parameters were used except for the temperature of application of the uniaxial pressure, which was gradually applied during the 600–1350 °C ramp for R0S and at 1350 °C for the present specimen A7. The study of shrinkage curves (not shown) reveals that the relative density at 1300 °C (assuming no reactions) is equal to 97% for R0S and only 68% for A. Thus, the formation of the Fe particles during the SPS treatment appears to be easier when the density of the compact remains low, during the heating, *i.e.* when the pressure is applied late as for specimen A7. This could reflect the possible role of open porosity in the process. Applying the pressure at low temperature may favor the closing of porosity before the formation of Fe by reaction (3) is thermally activated, which would decrease the possibility of O_2 leaving the sample and thus result in a thinner reaction zone and thus a thinner composite layer, as observed for R0S. This could also be related to the possibility that when the cross-sectional areas of particle–particle contacts are small, very high local current densities may be obtained, as suggested by other authors,[13,16] which may result in significantly higher local temperatures, which would also favor Fe formation by reaction (3) and the coalescence of Fe particles at the grain junctions of Al_2O_3, thus explaining the differences in particles size and the elongated shape observed for C7. This effect would be more prominent with pulse patterns producing higher crest intensities, as for specimen B7 (Fig. 1b) and most notably for specimen C7 (Fig. 1c). The results obtained with materials differing by their iron content (Fig. 3) support the above hypotheses. An increasing content of Fe^{3+} ions substituting for Al^{3+} ions can also be described as a higher hematite content dissolved into alumina,

up to the saturation reached for the sample with $x = 0.10$ as indicated in Section 2.1. The increasing saturation degree favors both reactions (1) and (3) at a given temperature. In samples with low iron contents (C2 and C5), differences in the kinetics of Fe^{3+} ions diffusion and $FeAl_2O_4$ formation by reaction (1) could explain the formation of the DL. By contrast, for C10 almost no DL is formed because the core contains a sufficient excess of Fe^{3+} ions to supply the top side in time. Moreover, as these specimens were prepared with the (2:6) pulse pattern ($I_c = 1722$ A), the microstructure evolution observed upon the increase of the iron content could be a consequence of changes in the local composition and on the local electrical conductivity, which would change local current densities, and possibly diffusion processes or local temperatures.

The graphite paper disks present between the punches and the powder could also play a role in helping to channel electrons into the sample. This could result in high local current densities or high local voltages in the material. The electrical conductivity of the solid solution, which is probably the limiting parameter for the penetration of current at some depth into the specimen, is probably quite low even at 1350 °C (10^{-7}–10^{-8} S/cm by comparison with data at 1500 and 1600 °C[30]). This would be in agreement with results on the distribution of current density within and around the material depending on its electrical conductivity.[16,31] Note that although modelling the electrical conductivity, iron cations diffusion and defect structure of such a material at high temperature and low $P(O_2)$ is fairly complex,[30] the electrical conductivity can be significantly higher than that of pure α-Al_2O_3. This could allow for the penetration of a higher current, and this deeper into the specimen, than what was reported for α-Al_2O_3.[32,33] Thus, electric discharge effects between grains and in closed porosities can not be ruled out. It was reported[34] that carbon coming by diffusion from the die is a reactant for the formation of W_2C during the SPS of W-Al_2O_3 composites. However, the presence of Fe_3C appears to be limited to the top-most surface and nothing was found to indicate that there is carbon diffusion along the whole sample as indicated in Ref. 34. Moreover, if carbon acted as a reactant, there would be a gradient in the presence of Fe particles within the composite layer (with more, and also larger, particles near the graphite paper), which is not observed. The role of carbon as a reactant for carburization and/or reduction, if any, does not extend very deep into the specimen (a few micrometers at most) and thus Fe^{3+} reduction by carbon or CO was ruled out as the main cause for the formation of the composite layer.

However, the above hypotheses fail to explain why, for the bottom size of specimen D7 (Fig. 4b), a large (64 μm) composite layer is formed above the DL, in an area not in contact with graphite. It is not possible to explain that reaction (3) would have occurred with such a clear separation from the core where reaction (1) took place because such a marked difference in temperature is not thought to be realistic. As noted above, the microstructure of this composite layer is different from the other ones, showing a lower density of larger Fe particles. This could reflect that the Fe particles originate from $FeAl_2O_4$ particles, *i.e.* they are formed by reaction (2). This is observed only for sample D7 because it is the only one prepared with a very long cycle. A very long treatment would probably transform all $FeAl_2O_4$ into Fe.

4. Conclusions

The influence of a key SPS parameter, the pulse current, was investigated on the sintering of reactive alumina–hematite solid solutions by varying the pulse pattern. For a given sintering cycle, changing the pulse pattern modifies the current crest intensities and has a great influence on the microstructure of the material. It is composed of a Fe-Al_2O_3 composite layer at the peripheral surfaces (top, bottom and radial), a biphased core ($FeAl_2O_4$ and Al_2O_3) and a depletion-layer (DL) without Fe nor $FeAl_2O_4$ between the composite layer and the core at the top side of the specimen, *i.e.* near the cathode. For long SPS treatment, there is also a DL at the very bottom side of the specimen. An important role of carbon (from the die or graphite paper disks) as a reactant was ruled out. However, graphite paper disks could play a role in helping to channel electrons into the sample, which could result in high local current densities or voltages in the material. Three main phenomena are in competition: formation of $FeAl_2O_4$ favored by lower $P(O_2)$ and higher temperatures, which is not peculiar to SPS, formation of Fe, producing Fe-Al_2O_3 composite layers of a regular thickness, and electrical-field induced diffusion of Fe^{3+} ions towards the cathode (*i.e.* upwards). To the best of our knowledge, this is the first time that such uni-directional cationic migration is observed during SPS densification of materials. This mechanism, linked to the potential gradient imposed by the SPS technique, is enhanced with the crest intensity of the applied current. The microstructure evolution with the change of pulse pattern could also reflect induced variations of local temperatures. These findings could have far-ranging implications for the SPS consolidation of ionic materials, for the *in situ* (reactive) shaping of novel composites and multimaterials. The formation of the Fe particles during the SPS treatment appears to be easier when the density of the compact remains low, during the heating, *i.e.* when the pressure is applied late, which could reflect the possible role of open porosity. Future works will include the study of the influence of porosity, notably to investigate surface effects, and the modelling of the current and temperature distributions along the stack.

Acknowledgements

The SPS was performed at the Plateforme Nationale CNRS de Frittage-Flash (PNF^2, Toulouse). Electron microscopy was performed at TEMSCAN, the "Service Commun de Microscopie Electronique", Université Paul-Sabatier. The authors thank J. Faber and Y. Paranthoen (Société des Céramiques Techniques, Bazet, France) for JGS doctoral thesis grant. This work is performed under the programme ANR-06-NANO-049.

References

1. Tokita M. Trends in advanced SPS Spark Plasma Sintering systems and technology. *J Soc Powder Technol* 1993;**30**(11):790–804.

2. Chaim R, Levin M, Shlayer A, Estournes C. Sintering and densification of nanocrystalline ceramic oxide powders: a review. *Adv Appl Ceram* 2008;**107**(3):159–69.
3. Artemenko A, Elissalde C, Chung U-C, Estournès C, Mornet S, Bykov I, et al. Linking hopping conductivity to giant dielectric permittivity in oxides. *Appl Phys Lett* 2010;**97**(13):132901–3.
4. Gurt Santanach J, Weibel A, Estournès C, Yang Q, Laurent Ch, Peigney A. Spark Plasma Sintering of alumina: parameters study, formal sintering analysis and hypotheses about the mechanism(s) involved in densification and grain growth. *Acta Mater* 2011;**59**(4):1400–8.
5. Marder R, Chaim R, Chevallier G, Estournès C. Effect of 1 wt% LiF additive on the densification of nanocrystalline Y_2O_3 ceramics by spark plasma sintering. *J Eur Ceram Soc* 2011;**31**(6):1057–66.
6. Millot N, Le Gallet S, Aymes D, Bernard F, Grin Y. Spark plasma sintering of cobalt ferrite nanopowders prepared by coprecipitation and hydrothermal synthesis. *J Eur Ceram Soc* 2007;**27**(2–3):921–6.
7. Kakegawa K, Suzuki SS, Uekawa N. Design of pyroelectric properties by controlling compositional distribution. *J Eur Ceram Soc* 2006;**26**(4–5):613–7.
8. Xu T, Wang P, Fang P, Kan Y, Chen L, Vleugels J, et al. Phase assembly and microstructure of CeO_2-doped ZrO_2 ceramics prepared by spark plasma sintering. *J Eur Ceram Soc* 2005;**25**(15):3437–42.
9. Shen ZJ, Johnsson M, Zhao Z, Nygren M. Spark plasma sintering of alumina. *J Am Ceram Soc* 2002;**85**(8):1921–7.
10. Shon IJ, Munir ZA. Synthesis of $MoSi_{2-x}Nb$ and $MoSi_{2-y}ZrO_2$ composites by the field-activated combustion method. *Mater Sci Eng A* 1995;**202**(1–2):256–61.
11. Tokita M. Development of large-size ceramic/metal bulk FGM fabricated by spark plasma sintering. *Mater Sci Forum* 1999;**308**(11):83–8.
12. Omori M. Sintering, consolidation, reaction and crystal growth by the spark plasma system. *Mater Sci Eng A* 2000;**287**(2):183–8.
13. Chaim R. Superfast densification of nanocrystalline oxide powders by Spark Plasma Sintering. *J Mater Sci* 2006;**41**(23):7862–71.
14. Chaim R, Marder-Jaeckel R, Shen JZ. Transparent YAG ceramics by surface softening of nanoparticles in spark plasma sintering. *Mater Sci Eng A* 2006;**429**(1–2):74–8.
15. Chaim R. Densification mechanisms in spark plasma sintering of nanocrystalline ceramics. *Mater Sci Eng A* 2007;**443**(1–2):25–32.
16. Anselmi-Tamburini U, Gennari S, Garay JE, Munir ZA. Fundamental investigations on the spark plasma sintering/synthesis process II. Modeling of current and temperature distributions. *Mater Sci Eng A* 2005;**394**(1–2):139–48.
17. Anselmi-Tamburini U, Garay JE, Munir ZA. Fundamental investigations on the spark plasma sintering/synthesis process. III. Current effect on reactivity. *Mater Sci Eng A* 2005;**407**(1–2):24–30.
18. Hulbert DM, Anders A, Andersson J, Lavernia EJ, Mukherjee AK. A discussion on the absence of plasma in spark plasma sintering. *Scripta Mater* 2009;**60**(10):835–8.
19. Munir ZA, Anselmi-Tamburini U, Ohyanagi M. The effect of electric field and pressure on the synthesis and consolidation of materials: a review of the spark plasma sintering method. *J Mater Sci* 2006;**41**(3):763–77.
20. Bernard-Granger G, Guizard C. Spark plasma sintering of a commercially available granulated zirconia powder. I. Sintering path and hypotheses about the mechanism(s) controlling densification. *Acta Mater* 2007;**55**(10):3493–504.
21. Bernard-Granger G, Addad A, Fantozzi G, Bonnefont G, Guizard C, Vernat D. Spark plasma sintering of a commercially available granulated zirconia powder: comparison with hot-pressing. *Acta Mater* 2010;**58**(9):3390–9.
22. Locci AM, Cincotti A, Todde S, Orru R, Cao G. A methodology to investigate the intrinsic effect of the pulsed electric current during the spark plasma sintering of electrically conductive powders. *Sci Technol Adv Mater* 2010;**11**(4):045005–45013.
23. Gurt Santanach J, Estournès C, Weibel A, Peigney A, Chevallier G, Laurent Ch. Sintering as a reactive sintering tool for the preparation of surface-tailored $Fe–FeAl_2O_4–Al_2O_3$ nanocomposites. *Scripta Mater* 2009;**60**(4):195–8.
24. Devaux X, Laurent Ch, Rousset A. Chemical Synthesis of metal nanoparticles dispersed in alumina. *Nanostruct Mater* 1993;**2**:339–46.
25. Chen W, Anselmi-Tamburini U, Garay JE, Groza JR, Munir ZA. Fundamental investigations on the Spark Plasma Sintering/Synthesis process. I. Effect of dc pulsing on reactivity. *Mater Sci Eng A* 2005;**394**(1–2):132–8.
26. Elrefaie FA, Smeltzer WW. Thermodynamics of the system iron–aluminum–oxygen between 1073 K and 1573 K. *Metall Trans B* 1983;**14**(1):85–93.
27. Tobi Even-Zur O, Chaim R. Effect of green density and electric field direction on densification of YAG nano-powders by Spark Plasma Sintering. *J Mater Sci* 2009;**44**(8):2063–8.
28. Devaux X, Laurent Ch, Brieu M, Rousset A. Iron–alumina interface in ceramic matrix nanocomposites. *J Alloys Compd* 1992;**188**(1–2):179–81.
29. Laurent Ch, Rousset A, Verelst M, Kannan KR, Raju AR, Rao CNR. Reduction behaviour of Fe^{3+}/Al_2O_3 obtained from the mixed oxalate precursor and the formation of the Fe^0-Al_2O_3 metal–ceramic composite. *J Mater Chem* 1993;**3**(5):513–8.
30. Koripella CR, Kröger FA. Electrical conductivity, diffusion of iron and the defect structure of α-Al_2O_3:Fe. *J Phys Chem Solids* 1986;**47**(6):565–8.
31. Makino Y. Characteristics of sintering process based on pulsed high current. *New Ceram* 1997;**10**:39–42.
32. Tomino H, Watanabe H, Kondo Y. Electric current path and temperature distribution for Spark Sintering. *J Jap Soc Powder Powder Metall* 1997;**44**(10):974–9.
33. Makino Y, Sakaguchi M, Trada J, Akamatsu K. Consolidation of ultrafine alumina powders with SPS method. *J Jap Soc Powder Powder Metall* 2007;**54**(4):219–25.
34. Rodriguez-Suarez T, Diaz LA, Torrecillas R, Lopez-Esteban S, Tuan WH, Nygren M, et al. Alumina/tungsten nanocomposites obtained by Spark Plasma Sintering. *Comp Sci Technol* 2009;**69**(14):2467–73.